Geophysical Research Letters

RESEARCH LETTER
10.1029/2023GL102825

Key Points:

- Upslope flow is intensified by a moving marine atmospheric boundary layer (MABL), with its features relying on a MABL's depth and density
- Upslope acceleration is enhanced by the MABL-induced perturbation pressure gradient force but is reduced over time by the negative buoyancy
- The passage of storm-generated high-frequency gravity waves and the associated surface pressure lows temporarily enhance the upslope flow

Supporting Information:

Supporting Information may be found in the online version of this article.

Correspondence to:
F. Wu,
fvw5116@psu.edu

Citation:
Wu, F., & Lombardo, K. (2023). The impact of offshore-propagating squall lines on coastal-mountain flows. *Geophysical Research Letters*, *50*, e2023GL102825. https://doi.org/10.1029/2023GL102825

Received 9 JAN 2023
Accepted 18 MAR 2023

The Impact of Offshore-Propagating Squall Lines on Coastal-Mountain Flows

Fan Wu[1] and **Kelly Lombardo**[1]

[1]Department of Meteorology and Atmospheric Science, The Pennsylvania State University, University Park, PA, USA

Abstract Dynamical physical processes associated with an onshore moving marine atmospheric boundary layer (MABL, i.e., sea breeze) over sloping terrain, sensitivity of these processes to MABL characteristics, and flow modifications induced by an offshore-moving squall line are investigated using idealized simulations. The moving MABL gradually advances inland, exhibiting farther advancement and greater upslope wind speed for deeper and cooler MABLs. The local acceleration is primarily driven by a MABL-generated perturbation pressure gradient force (PPGF). As the moving MABL air accumulates onshore over time, an opposing force associated with the increasing negative buoyancy eventually balances the PPGF and results in a quasi-steady upslope flow. The approaching squall line disrupts this flow in two distinct ways; Initially the storm's cold pool enhances the ambient downslope winds which diminishes the upslope wind speeds, and subsequently the storm-generated high-frequency waves and the associated surface pressure low enhances the upslope-directed PPGF which reintensifies the upslope flows.

Plain Language Summary This study uses numerical simulations to investigate the physical processes driving sea breezes over mountainous coastal regions, the sensitivity of the sea breeze evolution to its density and depth, and changes to the sea breeze by approaching organized deep convective storms (i.e., squall lines). Deeper and cooler marine atmospheric boundary layers move farther inland and have stronger wind speeds. The onshore upslope sea breeze is driven by an onshore-directed pressure gradient force (PGF) induced by the denser marine air. However, as the marine air accumulates onshore over time, its negative buoyancy drives an opposing offshore downslope force that helps to prevent any additional inland advancement of the sea breeze front. An offshore-moving squall line influences this flow in two ways; Squall line outflow initially weakens the sea breeze but then enhances the sea breeze by decreasing the surface pressure ahead of the sea breeze front through storm-induced gravity waves.

1. Introduction

Coastal regions with mountains along or near the land-sea boundary are often impacted by offshore-propagating organized deep convective systems such as squall lines (Futyan & Del Genio, 2007; Ichikawa & Yasunari, 2007; Kömüşçü et al., 1998; H. Li et al., 2021; Lombardo & Colle, 2012, 2013; Meng et al., 2013; Morel & Senesi, 2002). The interaction between a storm's cold pool and the ambient marine atmospheric boundary layer (MABL), which usually propagates inland as a density current (i.e., sea breeze), can initiate convection (CI) and/or enhance precipitation over coastal regions (e.g., a real case shown in Movie S1; Garstang et al., 1994; Huang, Liu, Liu, & Knievel, 2019; Huang, Liu, Liu, Li, & Knievel, 2019; Y. Li & Carbone, 2015; Lombardo, 2020; Wu & Lombardo, 2021). Previous studies found that the characteristics of the moving MABL (e.g., depth, thermal deficit) and its relationship to the coastal relief played a crucial role in the reintensification or decay of an offshore-moving squall line (Lombardo, 2020; Lombardo & Colle, 2013; Lombardo & Kading, 2018; Wu & Lombardo, 2021). However, the question remains, "How do mesoscale features associated with squall lines impact the ambient flow ahead of the storm over mountainous coastal regions, specifically in the presence of a sea breeze located in the mountain lee?," a pertinent question given that any modifications to the downstream flow can in turn impact the storm itself.

Observations of sea-breeze-mountain circulations, that is, the complex local circulations resulting from the interactions between sea-breeze and mountain-valley circulations, have been documented since the mid-twentieth century (Fosberg & Schroeder, 1966; Olsson et al., 1973). Much of the literature has explored this problem through the lens of a mountain modifying the sea breeze. For example, Doppler observations of coastal circulations over Monterey Bay, California, highlighted the horizontal variability of the sea breeze air during its development due to asymmetries induced by the coastal mountains (Banta, 1995; Banta et al., 1993). Mountains also influence the onshore progression of sea breeze flow. Upslope mountain flows augment the onshore sea breeze during the day, while drainage flows increase the offshore land breeze overnight (Bastin & Drobinski, 2006; Darby et al., 2002; Lu & Turco, 1994; Mahrer & Pielke, 1977; Ramis & Romero, 1995; Savijärvi & Matthews, 2004). These constructive additions of sea breeze and mountain flows are sensitive to the location of the mountains relative to the coastline, with a stronger coupling of the two circulations for mountains closer to coastlines (Lu & Turco, 1994). Mountain and sea-breeze circulations may also work in opposition during certain times in the diurnal cycle. In the late afternoon and early evening, for example, the developing mountain drainage flow may oppose the onshore sea breeze (Darby et al., 2002).

Squall lines are often initiated over coastal mountains and then move toward the coastline (Lombardo & Colle, 2011, 2012; Pucillo et al., 2019). The influence of an offshore-moving squall line on mountain-coastal circulations has not been investigated, though squall lines are known to modify the kinematics and thermodynamics of their surrounding environments (e.g., Fovell et al., 2006; Parker & Johnson, 2004). Over inland regions, mesoscale low surface pressures have been observed to form downwind of mesoscale convective systems (MCS; e.g., Fritsch & Chappell, 1980; Hoxit et al., 1976; Johnson & Hamilton, 1988), which can modify the near-surface flow field. Case study analyses of strong MCSs over the central United States illustrated a reduction in surface pressure due to compensating subsidence warming adjacent to the main convective line, which induced low-level convergence ahead of the existing storm (Hoxit et al., 1976). Downstream pressure lows and flow modifications can also be induced by high-frequency gravity waves excited by latent heat fluctuations within the convective line (Du et al., 2019; Fovell et al., 2006; Jiang, 2012); in the vicinity of mountains, gravity waves can also form as flow passes over the barrier (Houze, 2012). During the Boundary Layer Late Afternoon and Sunset Turbulence field campaign located in the lee of the Pyrenees Mountains (France), convectively-generated gravity waves associated with a MCS induced near-surface pressure and wind field oscillations as the waves propagated downstream of the MCS into the mountain lee (Román-Cascón et al., 2015). Despite the availability of fine spatiotemporal observations, the authors note that questions remain regarding the role of topography in the development of gravity waves and atmospheric variable signals. In contrast, role of MCS-generated gravity waves were minimal during an event in the lee of the Qinghai-Tibetan Plateau (China; Liang, 2022). The coupling of easterly upslope mountain flows and westerly mid-level winds were observed to excite terrain-locked gravity waves. As an MCS originating in the mountains moved down the mountain slope, it dissipated as it passed through the stationary descending branch of the gravity wave located in the mountain lee.

Based on observations, the impact of squall lines on mountain flows remains unclear. Further, fine spatiotemporal observations of squall lines moving over mountainous coastal regions are absent, and thus the impact of squall lines on stable sea breeze air masses in the mountain lee is unknown. Thus, we use idealized simulations to quantify the role of squall lines on coastal-mountain flows for sea breezes with a range of depth and thermal perturbation characteristics. The following section describes the numerical simulations designed to explore these physical processes, as well as the upslope momentum budget for quantitative analysis. In Section 3, simulations without and with an offshore-moving squall line are compared to highlight the impact of the storm on the physical processes driving the upslope coastal-mountain flows, including the role of convectively-generated gravity waves A summary is provided in Section 4.

2. Methods

2.1. Model Configuration

Numerical experiments are conducted using large-eddy idealized simulations with the Cloud Model 1 (CM1; Bryan & Fritsch, 2002). Simulations are performed in 3D with an 800-km (x direction) × 60-km (y direction) horizontal domain with 200-m grid spacing, and a 20-km vertical domain with grid spacing stretched from 50 m below 3 km to 250 m above 10 km. Open-radiative (Periodic) lateral conditions are applied to x (y) boundaries, with free slip conditions at the top and bottom boundaries. Morrison double-moment microphysical scheme is used to predict cloud droplets, cloud ice, rain, snow, and graupel (Morrison et al., 2009), and a TKE scheme is used to parameterize sub-grid turbulence (Deardorff, 1980). Radiation and surface fluxes are excluded to eliminate the time-varying impacts on MABL and squall line characteristics and to isolate the response of the moving MABL to the storm. Other configurations follow Wu and Lombardo (2021). Simulations are initialized with an analytic sounding based on observed profiles over mid-latitude coastal regions during sea-breeze-active seasons.

This sounding has been used in prior numerical studies quantifying the impact of moving MABLs on squall line evolution (Lombardo, 2020).

2.2. Experimental Design

A plateau-shaped mountain ($x = 0$–360 km) with a plateau height of 1.5 km and a 60-km slope ($x = 300$–360 km) is included as a simplified representation of observed coastal mountains, informed by observations of coastal orography (Wu & Lombardo, 2021). Initially, simulations are run for 6 hr with no MABL or squall line to allow the base-state winds to reach a quasi-steady state in the presence of terrain. After this spin-up period, the moving MABL is initialized as a stably stratified rectangular region of negative potential temperature perturbation (θ') over the plateau base ($x = 360$–800 km) and allowed to evolve over a 3-hr period. Sensitivity experiments use MABL depths of 500, 1,000, and 1,500 m and θ' of –3 and –5 K, with values constrained by coastal station observations during the warm season and informed by prior experiments (Lombardo & Kading, 2018; Wu & Lombardo, 2021). Finally, a squall line is initiated over the plateau top ($x = 200$ km) using a momentum forcing scheme (Morrison et al., 2015) as configured in Wu and Lombardo (2021), which matures and moves toward the coastline. Analyses are performed starting from the MABL initialization (i.e., $t = 0$) and divided into two stages: (T1) moving MABL evolution and (T2) MABL response to the squall line.

2.3. Momentum Budget Equation for Slope Winds

A mountain-oriented coordinate system (s, n) is used to analyze slope winds, with components along (s) and perpendicular (n) to the slope (Haiden, 2003; Mahrt, 1982). The transformed velocity components are

$$u_s = -u\cos\alpha + w\sin\alpha, \tag{1}$$

and

$$w_n = u\sin\alpha + w\cos\alpha, \tag{2}$$

where u_s is the along-slope wind with positive defined as upslope, w_n is the slope-normal wind with positive defined as perpendicularly away from the slope, and α is the slope angle.

The anelastic momentum equation (Wu & Lombardo, 2021) can be written as

$$\frac{d\mathrm{V}}{dt} = -\frac{1}{\overline{\rho}}\nabla p' + B\mathbf{k}, \tag{3}$$

where $\mathrm{V} = (u, v, w)$ is the wind field, p' ($\overline{p}$) is perturbation (base-state) pressure, $B \equiv -\rho' g/\overline{\rho}$ is buoyancy, ρ' ($\overline{\rho}$) is the perturbation (base-state) total density, g is the gravitational acceleration, and $\mathbf{k}$ is the vertical unit vector. The horizontal (e.g., x direction) and vertical components can be expressed, respectively, as

$$\frac{du}{dt} = -\frac{1}{\overline{\rho}}\frac{\partial p'}{\partial x} \tag{4}$$

and

$$\frac{dw}{dt} = -\frac{1}{\overline{\rho}}\frac{\partial p'}{\partial z} + B. \tag{5}$$

Since the rotated, terrain-following coordinate system is orthogonal, Equations 4 and 5 can be rewritten as "mixed" formulations of the momentum equation

$$\frac{du_s}{dt} = \frac{1}{\overline{\rho}}\frac{\partial p'}{\partial x}\cos\alpha + \left(-\frac{1}{\overline{\rho}}\frac{\partial p'}{\partial z} + B\right)\sin\alpha, \tag{6}$$

and

$$\frac{dw_n}{dt} = -\frac{1}{\overline{\rho}}\frac{\partial p'}{\partial x}\sin\alpha + \left(-\frac{1}{\overline{\rho}}\frac{\partial p'}{\partial z} + B\right)\cos\alpha, \tag{7}$$

with accelerations in the (s, n) system but expressed in terms of derivatives in the (x, z) system (Haiden, 2003). Applying the derivative relationships in the rotated coordinate, Equations 6 and 7 can be converted to a purely (s, n) system

$$\frac{du_s}{dt} = -\frac{1}{\rho}\frac{\partial p'}{\partial s} + B\sin\alpha, \tag{8}$$

and

$$\frac{dw_n}{dt} = -\frac{1}{\rho}\frac{\partial p'}{\partial n} + B\cos\alpha. \tag{9}$$

Thus, along-slope acceleration can be regarded as the sum of along-slope perturbation pressure gradient force (PGF) and along-slope component of buoyancy (Equation 8). Under *quasi-hydrostatic equilibrium* for small slope angles ($\alpha < 10°$), the RHS of Equation 9 is ~0 (Haiden, 2003; Mahrt, 1982). Expanding Equation 8 gives

$$\underbrace{\frac{\partial u_s}{\partial t}}_{\substack{\text{local}\\ \text{change}}} = \underbrace{-u_s\frac{\partial u_s}{\partial s} - w_n\frac{\partial u_s}{\partial n}}_{\text{advection}} \underbrace{-\frac{1}{\rho}\frac{\partial p'}{\partial s}}_{\text{PGF}} + \underbrace{B\sin\alpha}_{\text{buoyancy}}. \tag{10}$$

The LHS of Equation 10 is the local change for upslope wind speed u_s, and the RHS terms are the accelerations contributing to the local change (from left to right): along-slope advection, slope-normal advection, along-slope PGF, and along-slope buoyancy.

3. Results

The evolutions of the moving MABLs' wind speeds, particularly wind speed sensitivity to MABL depth and thermal deficit, are evaluated through time series of u_s (i.e., upslope wind speed; Figure 1). All moving MABLs reach their peaks in onshore upslope wind speed within 90 min, with earlier peak times for deeper and cooler MABLs. The magnitudes of u_s are sensitive to the MABLs' characteristics, exhibiting greater enhancements of upslope flows for primarily deeper, and secondarily cooler, MABLs (Figure 1). Following, the upslope wind speeds slowly decline and reach quasi-steady flow speeds at the end of T1 (180 min). With no squall line, this quasi-steady flow continues through period T2 (Figure 1a). However, the inclusion of a squall line dramatically alters the flows (Figure 1b). Between 180 and 230 min, flows transition to downslope flow, with values as large as –5 m s^{-1} for the CTRL (no MABL) and 500-m deep MABLs. From 235 to 275 min, the upslope flows recover, with winds 0.78–2.88 m s^{-1} larger than seen in the absence of the storm. After 275 min, upslope wind speeds rapidly decline caused by the squall line's descending cold pool outflow. The following subsections analyze the related dynamic physical processes governing these flows and flow transitions during T1 and T2. The whole evolution of upslope flows from 0 to 360 min can be found in Movies S2 and S3, and the associated variations in magnitude and structure of upslope winds can be found in Movie S4.

3.1. Physical Processes Associated With Upslope Moving MABLs

The upslope flows in these simulations are composed of a mountain circulation formed because of the westerly ambient winds and an inland moving MABL (Bastin & Drobinski, 2006; Poulos et al., 2000, 2007). Weak upslope mountain flow forms during the 6-hr spin-up period because the downsloping ambient winds produce a positive buoyancy anomaly through adiabatic warming over the middle of the mountain slope (black dashed contours in Figure 2) and thus generate an upslope PPGF. Within 1 hr after the insertion of the MABL, the onshore movement of the negatively buoyant marine air intensifies the upslope flow over the lower slope (x = 330–360 km), with larger local accelerations (i.e., positive local tendency) associated with deeper and colder MABLs (Figure 2), consistent with the wind speed magnitudes in Figure 1. Additionally, these more robust MABLs advance farther inland, with onshore advancements progressively increasing from 15 to 17 km for the 500-m deep MABL, 20–25 km for the 1,000-m deep MABL, to 22–28 km for the 1500-m deep MABL. Marine atmospheric boundary layer thermal deficits primarily influence the magnitude of upslope accelerations rather than the inland advancement, with 0.26–4.20 × 10^{-4} m s^{-2} larger accelerations for -5-K-θ' MABLs than -3-K-θ' MABLs (Figure 2).

The contributions to these differences in upslope acceleration over the lower portion of the mountain slope (i.e., location of the onshore moving MABL air) are analyzed through a momentum budget. For the shallow MABLs (500-m deep), their upslope accelerations are the lowest because of the competing forces between the positive

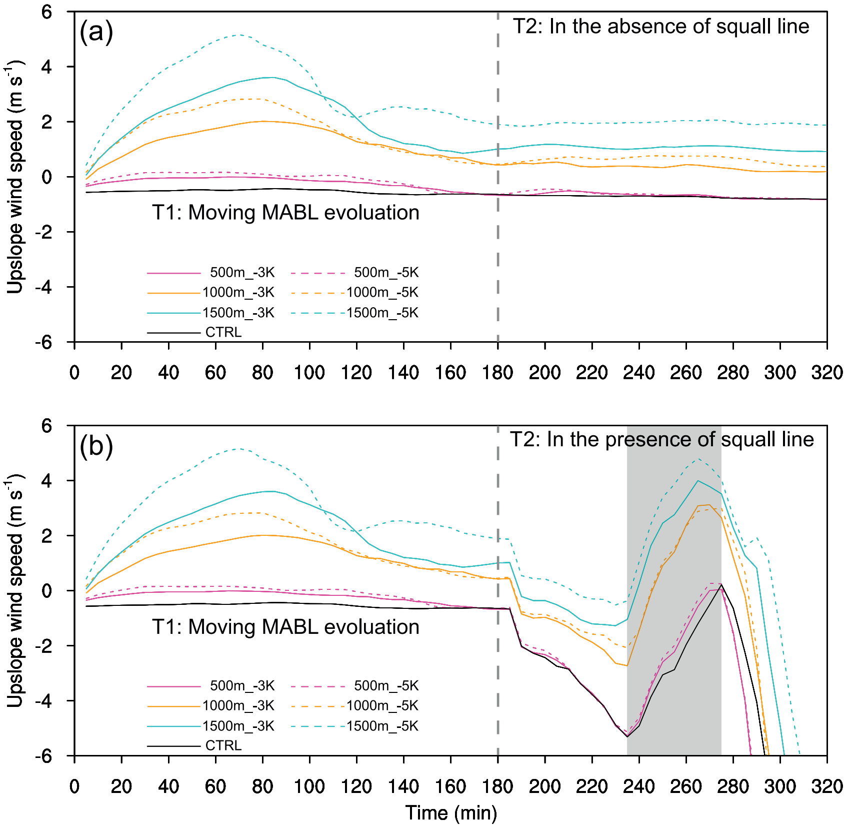

Figure 1. Time series of upslope wind speed (m s^{-1}) averaged from the ground to 500 m AGL over the lower slope (330–360 km) for the CTRL experiment (black) and experiments with a marine atmospheric boundary layer (MABL) (θ' of –3 K and –5 K are represented by solid lines and dashed lines, respectively, and depths of 500 m, 1,000 m, and 1,500 m are represented by magenta, orange, and blue lines, respectively) (a) in the absence of and (b) in the presence of a squall line. The evolutions of the moving MABL from 0 to 180 min (T1) are the same in (a, b). The periods of decreasing upslope flow (180–230 min) and increasing upslope flow (235–275 min, shaded) in (b) are analyzed in Section 3.2.

PGF and the negative advection and buoyancy forces (Figures 2a and 2b). The PGF forms due to the pressure gradient between a relative surface high pressure associated with the dense MABL air and a pressure low that develops over the middle slope ($x = 320$–330 km) associated with the adiabatic warming of downsloping ambient air (Figures 2a and 2b). Given that the pressure low magnitude and location are constant among simulations due to its formation mechanism, the upslope PGF magnitude is determined by the MABL thermal deficit, with a larger pressure and thus a 1.81×10^{-4} m s^{-2} greater PGF for −5-K-θ' MABL than –3-K-θ' MABL. However, the cooler MABL air is more negatively buoyant and creates a larger negative buoyancy acceleration (–0.42 × 10^{-3} m s^{-2}; Figure 2b), muting the influence of the PGF. Advection is negative due to the presence of downsloping ambient winds over the lower slope during the earlier part of the temporal averaging period.

For the 1000-m deep MABLs, the deeper marine layers augment the upslope pressure gradients and result in 3.67×10^{-4} m s^{-2} greater PGF in the –5-K-θ' MABL, though this simultaneously creates a –5.16 × 10^{-4} m s^{-2} larger negative buoyancy force (Figures 2c and 2d). Given that the upslope flow associated with the sea breeze arrives over the lower slope sooner than in the 500-m deep MABL simulations, the impact of the ambient downslope winds on the advection term is smaller, transitioning to a positive upslope contribution for the –5-K-θ' MABL (0.13×10^{-3} m s^{-2}; Figure 2d) associated with the advection of the marine air toward the slope after initialization. The trend toward a positive advection contribution helps support the larger upslope accelerations (0.70×10^{-3} m s^{-2}) regardless of the enhanced negative buoyancy force (–1.06 × 10^{-3} m s^{-2}). As a result, local accelerations increase in the 1000-m deep MABLs, consistent with the larger magnitude (1.75–2.67 m s^{-1}) in upslope flow (Figure 1a). For the deepest (1,500-m deep) MABLs, these trends continue in the PGF, buoyancy, advection, and local acceleration (Figures 2e and 2f). After 60 min in all experiments, upslope flow magnitude (Figure 1) and acceleration (not shown) begin to decline due to a continued enhancement in the negative

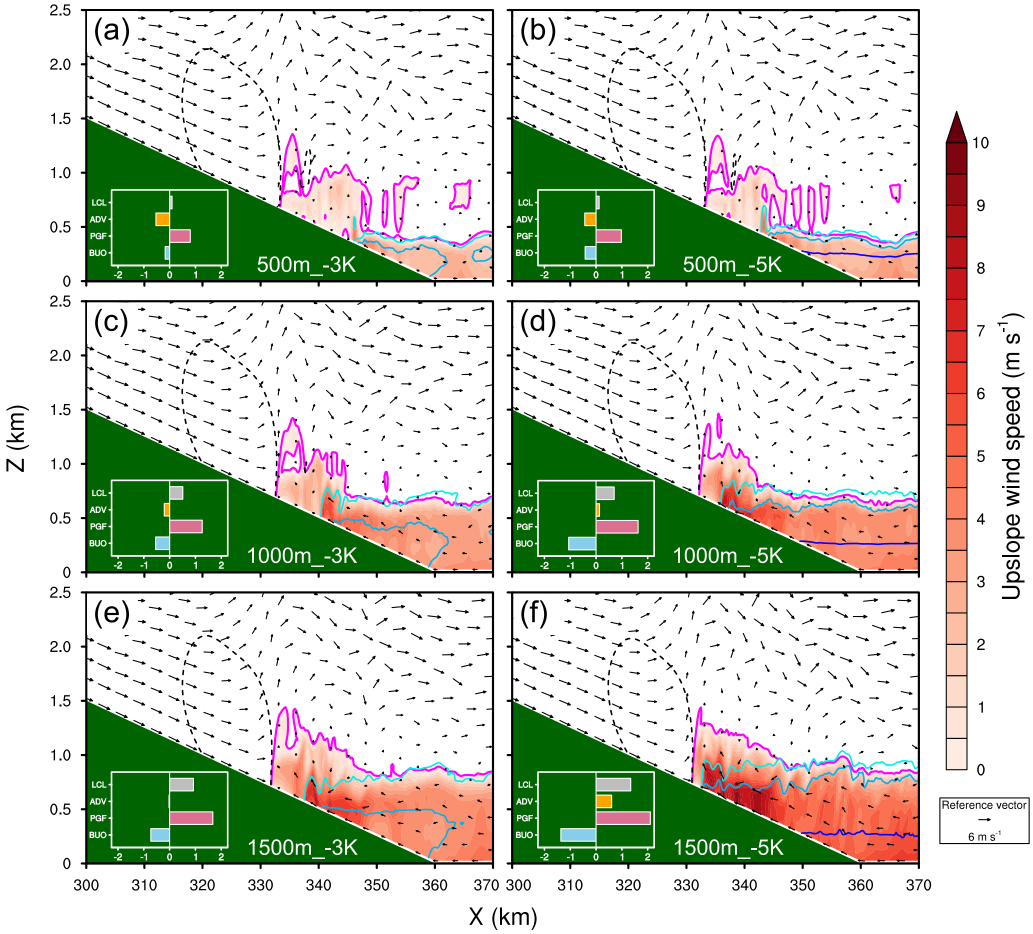

Figure 2. Cross-sections of 0–60 km y-averaged upslope ($u_s > 0$) wind speed (m s^{-1}, shaded and bounded by magenta contours), buoyancy of –0.15 m s^{-2} (deep blue contour), –0.10 m s^{-2} (blue contour), –0.05 m s^{-2} (light blue contour) and 0.05 m s^{-2} (black dashed contour), and *u-w* wind vectors (m s^{-1}, reference vector 6 m s^{-1}) at 60 min for experiments with a –3-K-θ' (a) 500-m deep, (c) 1,000-m deep, (e) 1,500-m deep marine atmospheric boundary layer (MABL), and a –5-K-θ' (b) 500-m deep, (d) 1000-m deep, (f) 1500-m deep MABL. Terrain is shaded in dark green. Bar charts of the local change of u_s (LCL, 10^{-3} m s^{-2}, gray), and the budget terms including advection (ADV, 10^{-3} m s^{-2}, orange), perturbation pressure gradient force (PGF, 10^{-3} m s^{-2}, pink), and buoyancy (BUO, 10^{-3} m s^{-2}, blue) accelerations averaged from the ground to 500 m AGL over 330–360 km during 0–60 min are displayed in the inset.

buoyancy acceleration as the MABL air accumulates over the lower slope. Once the negative buoyancy force is balanced by the advective and pressure gradient forces, the upslope flow reaches a quasi-steady state (not shown).

3.2. Response of the Moving MABLs to an Approaching Squall Line

The mechanisms controlling the disruption to this quasi-steady flow by the offshore-moving squall line are presented for experiments with the weakest MABL (500-m deep, –3-K θ') and the most intense MABL (1,500-m deep, –5-K θ') for contrast. At 210 min, a mature squall line is located at 240 km (Figures 3a and 3b), and the upslope flow over the lower slope transitions to downslope (Figure 1b) in both simulations (Movie S5). Local accelerations are more negative in the shallow-MABL simulation (–0.89 × 10^{-3} m s^{-2}) than the deep MABL simulation (–0.38 × 10^{-3} m s^{-2}; Figures 3c and 3d), consistent with the strong downslope and near zero wind speeds, respectively (Figure 1b). Compared with the simulations with no squall line (Movie S6), both experiments show increased downslope winds due to the squall line outflow, contributing to more negative advection terms. Therefore, the outflow of the approaching squall line modifies the downstream wind fields, decelerating the upslope flows associated with the moving MABLs.

When the squall line reaches the plateau top edge by 260 min (Figures 3e–3h), the upslope flows redevelop and thereafter become more intense than in the no-squall-line simulations, with an increases of 0.78–2.88 m s^{-1} in

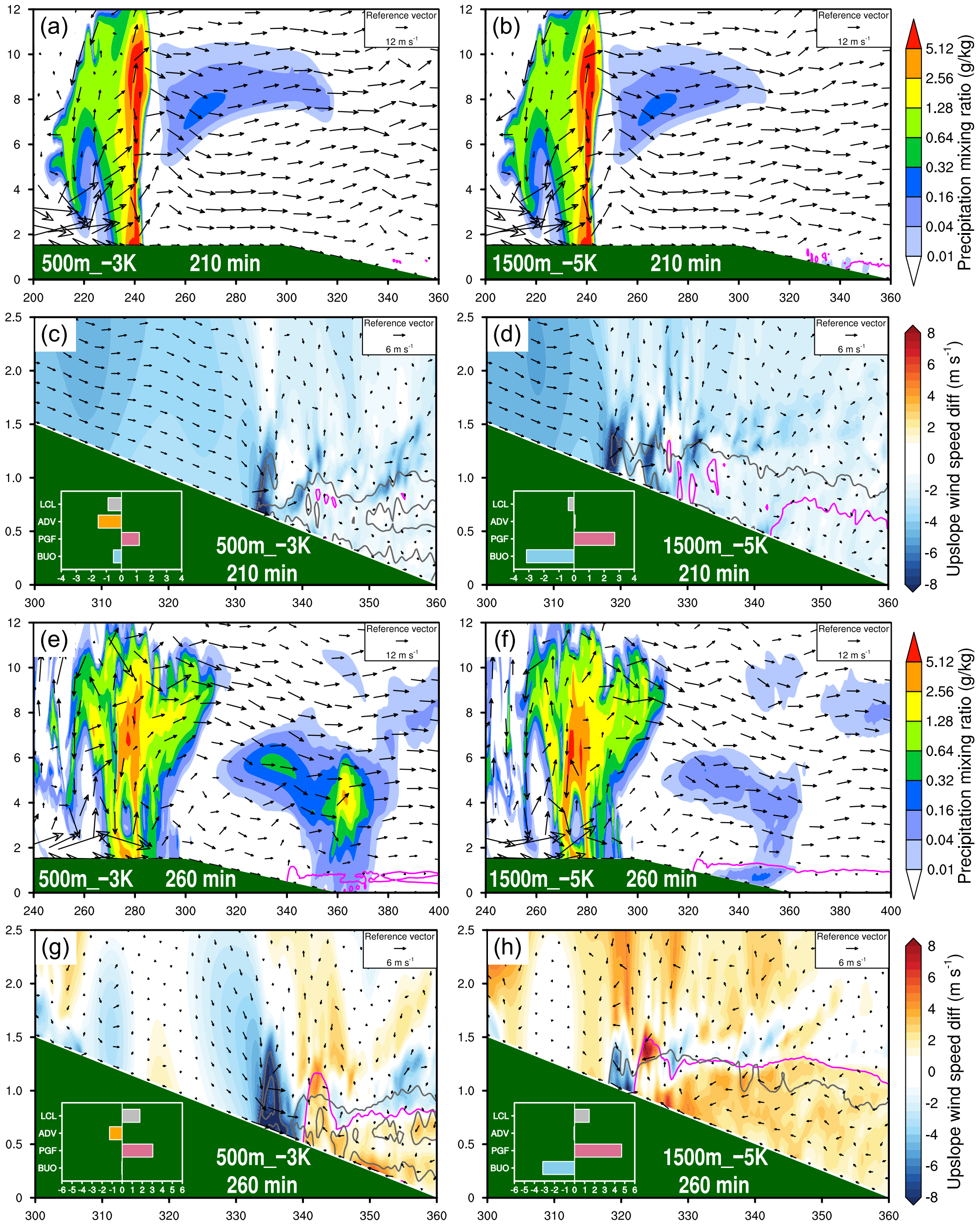

Figure 3. Cross-sections of 0–60 km y-averaged precipitation mixing ratio (shaded, g kg^{-1}), u-w wind vectors (m s^{-1}, reference vector 12 m s^{-1}), and upslope ($u_s > 0$) wind speed (m s^{-1} bounded by magenta contours) at 210 min for experiment with a (a) 500-m-deep, –3-K-θ' marine atmospheric boundary layer (MABL) and (b) 1,500-m-deep, –5-K-θ' MABL in the presence of a squall line. (c, d) Zoomed-in cross sections of upslope flow bounded by magenta (gray) contours in the presence (absence) of a squall line, upslope wind speed difference (shaded, m s^{-1}) between simulations with a squall line and with no squall line, and difference of u-w wind vectors (m s^{-1}, reference vector 6 m s^{-1}). Panels (e–h) are the same as (a, b) but at 260 min. Terrain is shaded dark green. Bar charts in the inset are the same as Figure 2 but the experiments with a squall line averaged from (c, d) 180–230 min and (g, h) 235–275 min.

upslope wind speed (Figure 1). The local acceleration shows enhancements in the 500-m and 1,500-m deep MABL experiments, partly due to a rise in the PGF (Figures 3g and 3h). To address this transition, we present pressure perturbations (p') associated with the squall line for the experiment with a 500-m-deep, –3-K-θ' MABL as an example (other MABL experiments with similar results are not shown). While the mature squall line is located over the plateau top, a low p' forms near the surface in front of its cold pool by 210 min (Figure 4a), which propagates eastward away from the storm at a ground-relative phase speed of ∼35 m s^{-1} between 215 and 230 min (Figures 4b–4e). This low p' forms underneath and in response to a region of enhanced warming, displayed as a maximum in potential temperature perturbation (θ') centered at ∼4 km in altitude (indicated by "A" in Figures 4b–4e). The low-level warming and associated low p' reflect the propagation of a high-frequency gravity wave, specifically the thermal response to the descending branch of the wave (e.g., Koch & O'Handley, 1997; Ralph et al., 1993), that develops in response to fluctuations in convective storm latent heating (e.g., Halliday et al., 2018; Liu & Moncrieff, 2004; Yanai et al., 1973). These features are independent of the downslope adiabatic warming (indicated by "B" in Figure 4e) discussed in Section 3.1.

Comparison of time series of the near-surface pressure perturbation (p') over the slope (320–340 km in x) and near the mountain base (340–360 km in x) illustrate the impact of the convectively-generated surface low on the coastal-mountain flow (Figure 4i). Between 210 and 230 min, the gravity wave is located over the plateau top imparting no influence on the p' distribution over the slope at this time. Consequently, the difference in p' over the slope versus the mountain base is minimal (0.22–0.32 hPa) and the resultant PPGF contribution (0.88–2.00 × 10^{-3} m s^{-2}) is small (Figure 4i). As the gravity wave propagates eastward, its low p' reaches the upper slope at 235 min (Figure 4f), which decreases the over-slope p', creating a 0.71 hPa p' difference along the slope and a positive (upslope) PPGF (Figure 4i). The along-slope p' difference and PPGF continue to increase, maximizing at 245 min (1.40 hPa and 7.13 × 10^{-3} m s^{-2}, respectively). At this time, the gravity-wave induced surface low is p' collocated with the terrain-induced low p' caused by downslope adiabatic warming. Due to this localized reduction in surface p' associated with the addition of the two low p' centers, upslope flow redevelops with a dramatic surge in speed beginning at 235 min (Figure 1b). As the gravity wave moves over the mountain base, its surface low p' merges with the high p' associated with the dense sea breeze air (Figure 4h), resulting in a reduction in the along-slope p' difference (0.38 hPa) and PPGF (2.14 × 10^{-3} m s^{-2}) at 250 min (Figure 4i). However, a new convectively-generated gravity wave (indicated by "C") begins to descend the slope after 250 min (Figure 4h). The associated surface low p' enhances the along-slope p' difference (0.67 hPa) and PPGF (3.82 × 10^{-3} m s^{-2}) once again at 255 min (Figure 4i), supporting a persistent upslope flow (Figure 1b). By 275 min, this second gravity moves over the mountain base and the pressure signals are dominated by the passage of the squall line cold pool outflow; the associated surface high p' now located over the slope reverses the along-slope PPGF and drives a downslope flow (Figures 1b and 4i).

4. Conclusions

This study utilized idealized simulations to investigate the response of upslope moving MABLs (i.e., sea breezes) to an approaching squall line in a mountainous coastal environment. The work built on our prior research that highlighted the important role played by a moving MABL in a squall line's evolution (Lombardo, 2020; Lombardo & Kading, 2018; Wu & Lombardo, 2021). Here, we quantified the sensitivity of upslope flow to characteristics of the onshore moving MABL air as well as the impact of a near proximity squall line on the upslope marine flow characteristics, which in turn can influence squall line evolution. The upslope flow characteristics were dominated by the depth and density of the marine air. The inland advancement and intensity of the upslope winds depended on the depth and thermal deficit θ' of the marine air. Generally, deeper and cooler MABLs advanced farther inland and had greater upslope wind speeds, with flow magnitudes primarily sensitive to MABL depth. The local upslope flow was accelerated by a PGF that arose due to the pressure gradient between a high perturbation pressure from the dense marine air over the lower slope and a low perturbation pressure from adiabatic warming of ambient downslope winds over the upper slope. An opposing negative buoyancy acceleration developed over time as the dense marine air accumulated over the lower slope. Consequently, the upslope flows decelerated and eventually reached a quasi-steady state.

An offshore-moving squall line disrupted the quasi-steady marine flow in two distinct ways. Initially, squall line outflow diminished the marine flow and resulted in either no flow or downslope flow over the lower mountain slope, sensitive to MABL characteristics. Subsequently, storm-generated high-frequency gravity waves created surface low perturbation pressure. As the low pressure propagated away from the squall line and approached the low perturbation pressure over the upper slope due to adiabatic warming of downslope ambient winds, the PGF rapidly increased, and winds surged up the slope. Such a change in wind speed has the potential to influence a squall line's behavior and the associated precipitation over the mountainous coastal regions.

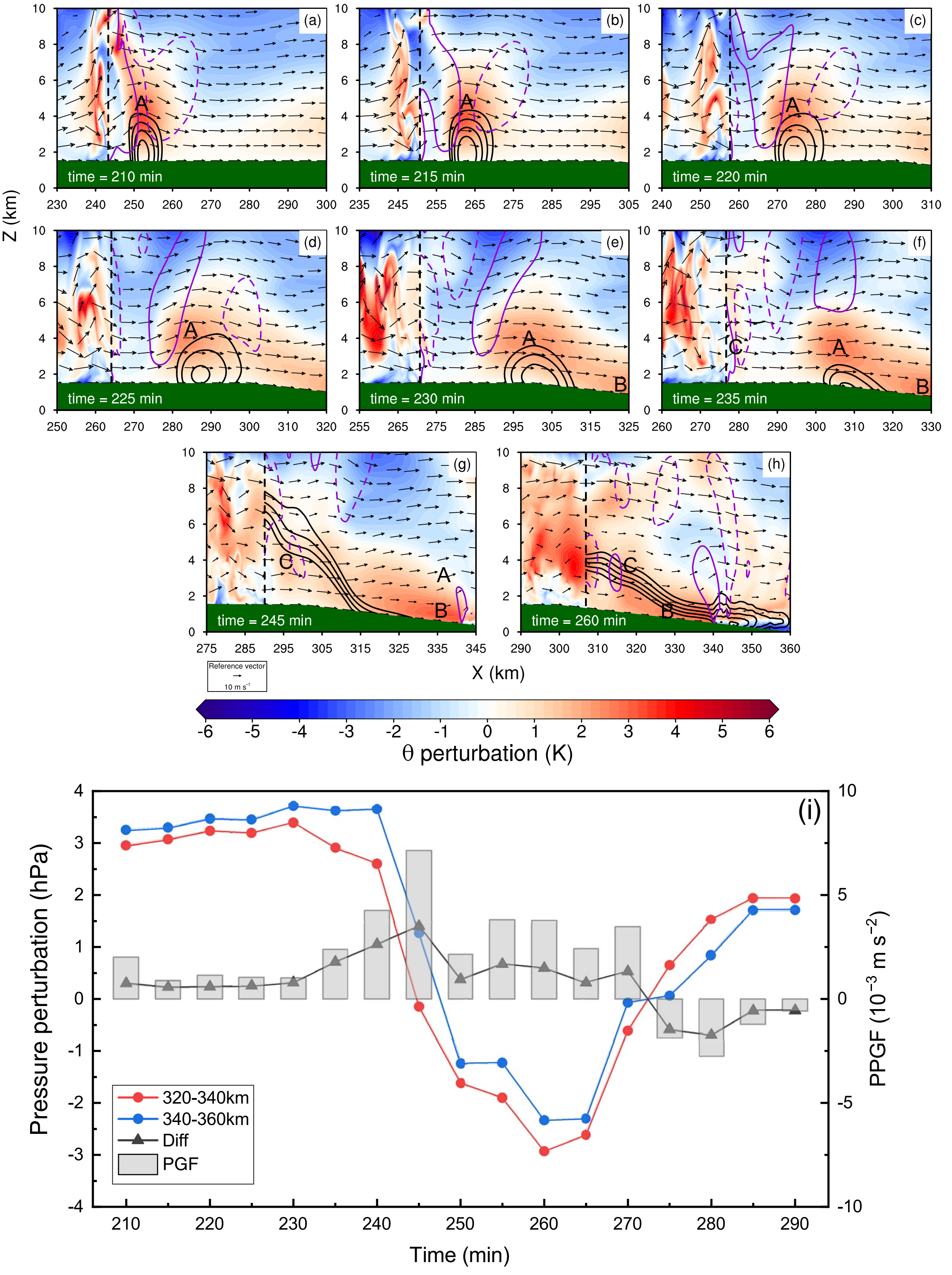

Figure 4. Cross-sections of 0–60 km y-averaged potential temperature perturbation (θ', shaded, K), normalized pressure perturbation (black contours of –0.25, –0.20, –0.15, –0.10, –0.05), vertical velocity of –1.0 m s^{-1} (1.0 m s^{-1}) indicated by purple dashed (solid) contours, and *u-w* wind vectors (m s^{-1}, reference vector 10 m s^{-1}) from (a–h) 210–260 min for the simulation with a 500-m-deep, –3-K-θ' marine atmospheric boundary layer, and (i) time series of pressure perturbations (hPa) averaged from the ground to 500 m AGL over 320–340 km in *x* (red line) and 340–360 km in *x* (blue line), their difference (hPa; gray line), and the perturbation pressure gradient force (PPGF) budget term as in Equation 10 (10^{-3} m s^{-2}; Gy bars) contributing to the local change of u_s averaged from the ground to 500 m AGL over 340–360 km in *x*. Cold pool leading edge is indicated by black dashed line. Temperature anomalies associated with gravity waves are marked with "A" and "C," and with downslope winds is indicated by "B." In panels g–h, the perturbation pressure magnitude associated with A is smaller than that associated with C, and thus feature C dominates the normalized perturbation pressure field.

Future work should verify the proposed mechanisms in observations, though such observations are required at high spatiotemporal frequencies. In lieu of this, additional simulations with more realistic topography and a wider range of environmental soundings could help to bridge further the gap between idealized studies such as this one and observed storms. Additionally, the inclusion of radiation, surface fluxes, and a diurnal cycle will influence the magnitude of both the storm and marine air, potentially illustrating the sensitivity of these processes to the time of day. Finally, the results presented herein provide a benchmark for future studies using more complex mountain configurations with time-varying factors.

Data Availability Statement

The CM1 (version 20.3) numerical code used in this work is available at https://www2.mmm.ucar.edu/people/bryan/cm1/. The analytic sounding used to initialize the simulations is openly available at https://doi.org/10.5281/zenodo.5576899.

Acknowledgments
This research would not have been possible without the generous support from the National Science Foundation Award #AGS-1514115, Office of Naval Research Award #N00014-16-1-3199, Office of Naval Research Award #N00014-17-1-2478, and National Atmospheric and Oceanographic Administration Award #NA19OAR4590222. The authors appreciate the feedback provided by two anonymous reviewers, which improved the clarity of the manuscript. The authors also greatly thank Dr. George Bryan for the development of and continued improvements to the CM1. Numerical simulations for this research were performed on the Pennsylvania State University's Institute for Computational and Data Sciences' Roar supercomputer.

References

Banta, R. M. (1995). Sea breezes shallow and deep on the California Coast. *Monthly Weather Review*, *123*(12), 3614–3622. https://doi.org/10.1175/1520-0493(1995)123<3614:SBSADO>2.0.CO;2

Banta, R. M., Olivier, L. D., & Levinson, D. H. (1993). Evolution of the Monterey Bay sea-breeze layer as observed by pulsed Doppler lidar. *Journal of the Atmospheric Sciences*, *50*(24), 3959–3982. https://doi.org/10.1175/1520-0469(1993)050<3959:EOTMBS>2.0.CO;2

Bastin, S., & Drobinski, P. (2006). Sea-breeze-induced mass transport over complex terrain in south-eastern France: A case-study. *Quarterly Journal of the Royal Meteorological Society*, *132*(615), 405–423. https://doi.org/10.1256/qj.04.111

Bryan, G. H., & Fritsch, J. M. (2002). A benchmark simulation for moist nonhydrostatic numerical models. *Monthly Weather Review*, *130*(12), 2917–2928. https://doi.org/10.1175/1520-0493(2002)130<2917:ABSFMN>2.0.CO;2

Darby, L. S., Banta, R. M., & Pielke, R. A. (2002). Comparisons between mesoscale model terrain sensitivity studies and Doppler lidar measurements of the sea breeze at Monterey Bay. *Monthly Weather Review*, *130*(12), 2813–2838. https://doi.org/10.1175/1520-0493(2002)130<2813:CBMMTS>2.0.CO;2

Deardorff, J. W. (1980). Stratocumulus-capped mixed layers derived from a three-dimensional model. *Boundary-Layer Meteorology*, *18*(4), 495–527. https://doi.org/10.1007/BF00119502

Du, Y., Rotunno, R., & Zhang, F. (2019). Impact of vertical wind shear on gravity wave propagation in the land–sea-breeze circulation at the equator. *Journal of the Atmospheric Sciences*, *76*(10), 3247–3265. https://doi.org/10.1175/JAS-D-19-0069.1

Fosberg, M. A., & Schroeder, M. J. (1966). Marine air penetration in Central California. *Journal of Applied Meteorology*, *5*(5), 573–589. https://doi.org/10.1175/1520-0450(1966)005<0573:MAPICC>2.0.CO;2

Fovell, R. G., Mullendore, G. L., & Kim, S. H. (2006). Discrete propagation in numerically simulated nocturnal squall lines. *Monthly Weather Review*, *134*(12), 3735–3752. https://doi.org/10.1175/MWR3268.1

Fritsch, J. M., & Chappell, C. F. (1980). Numerical prediction of convectively driven mesoscale pressure systems. Part II. Mesoscale model. *Journal of the Atmospheric Sciences*, *37*(8), 1734–1762. https://doi.org/10.1175/1520-0469(1980)037<1734:NPOCDM>2.0.CO;2

Futyan, J. M., & Del Genio, A. D. (2007). Deep convective system evolution over Africa and the Tropical Atlantic. *Journal of Climate*, *20*(20), 5041–5060. https://doi.org/10.1175/JCLI4297.1

Garstang, M., Massie, H. L., Halverson, J., Greco, S., & Scala, J. (1994). Amazon coastal squall lines. Part I: Structure and kinematics. *Monthly Weather Review*, *122*(4), 608–622. https://doi.org/10.1175/1520-0493(1994)122<0608:ACSLPI>2.0.CO;2

Haiden, T. (2003). On the pressure field in the slope wind layer. *Journal of the Atmospheric Sciences*, *60*(13), 1632–1635. https://doi.org/10.1175/1520-0469(2003)60<1632:OTPFIT>2.0.CO;2

Halliday, O. J., Griffiths, S. D., Parker, D. J., Stirling, A., & Vosper, S. (2018). Forced gravity waves and the tropospheric response to convection. *Quarterly Journal of the Royal Meteorological Society*, *144*(712), 917–933. https://doi.org/10.1002/qj.3278

Houze, R. A. (2012). Orographic effects on precipitating clouds. *Reviews of Geophysics*, *50*(1), RG1001. https://doi.org/10.1029/2011RG000365

Hoxit, L. R., Chappell, C. F., & Michael Fritsch, J. (1976). Formation of mesolows or pressure troughs in advance of cumulonimbus clouds. *Monthly Weather Review*, *104*(11), 1419–1428. https://doi.org/10.1175/1520-0493(1976)104<1419:FOMOPT>2.0.CO;2

Huang, Y., Liu, Y., Liu, Y., & Knievel, J. C. (2019a). Budget analyses of a record-breaking rainfall event in the coastal metropolitan city of Guangzhou, China. *Journal of Geophysical Research: Atmospheres*, *124*(16), 9391–9406. https://doi.org/10.1029/2018JD030229

Huang, Y., Liu, Y., Liu, Y., Li, H., & Knievel, J. C. (2019b). Mechanisms for a record-breaking rainfall in the coastal metropolitan city of Guangzhou, China: Observation analysis and nested very large eddy simulation with the WRF Model. *Journal of Geophysical Research: Atmospheres*, *124*(3), 1370–1391. https://doi.org/10.1029/2018JD029668

Ichikawa, H., & Yasunari, T. (2007). Propagating diurnal disturbances embedded in the Madden-Julian Oscillation. *Geophysical Research Letters*, *34*(18), L18811. https://doi.org/10.1029/2007GL030480

Jiang, Q. (2012). On offshore propagating diurnal waves. *Journal of the Atmospheric Sciences*, *69*(5), 1562–1581. https://doi.org/10.1175/JAS-D-11-0220.1

Johnson, R. H., & Hamilton, P. J. (1988). The relationship of surface pressure features to the precipitation and airflow structure of an intense midlatitude squall line. *Monthly Weather Review*, *116*(7), 1444–1473. https://doi.org/10.1175/1520-0493(1988)116<1444:TROSPF>2.0.CO;2

Koch, S. E., & O'Handley, C. (1997). Operational forecasting and detection of mesoscale gravity waves. *Weather and Forecasting*, *12*(2), 253–281. https://doi.org/10.1175/1520-0434(1997)012<0253:OFADOM>2.0.CO;2

Kömüşçü, A. Ü., Erkan, A., & Çelik, S. (1998). Analysis of meteorological and terrain features leading to the Izmir flash flood, 3–4 November 1995. *Natural Hazards*, *18*(1), 1–25. https://doi.org/10.1023/A:1008078920113

Li, H., Huang, Y., Hu, S., Wu, N., Liu, X., & Xiao, H. (2021). Roles of terrain, surface roughness, and cold pool outflows in an extreme rainfall event over the coastal region of South China. *Journal of Geophysical Research: Atmospheres*, *126*(23), 1–28. https://doi.org/10.1029/2021JD035556

Li, Y., & Carbone, R. E. (2015). Offshore propagation of coastal precipitation. *Journal of the Atmospheric Sciences*, *72*(12), 4553–4568. https://doi.org/10.1175/JAS-D-15-0104.1

Liang, Z. (2022). Influence of the interaction between different low- and mid-level wind couplings and orography on the evolution of mesoscale convective systems in northwest China: A case study. *Quarterly Journal of the Royal Meteorological Society*, *148*(747), 3010–3032. https://doi.org/10.1002/qj.4350

Liu, C., & Moncrieff, M. W. (2004). Effects of convectively generated gravity waves and rotation on the organization of convection. *Journal of the Atmospheric Sciences*, *61*(17), 2218–2227. https://doi.org/10.1175/1520-0469(2004)061<2218:EOCGGW>2.0.CO;2

Lombardo, K. A. (2020). Squall line response to coastal Mid-Atlantic thermodynamic heterogeneities. *Journal of the Atmospheric Sciences*, *77*(12), 4143–4170. https://doi.org/10.1175/JAS-D-20-0044.1

Lombardo, K. A., & Colle, B. A. (2011). Convective storm structures and ambient conditions associated with severe weather over the Northeast United States. *Weather and Forecasting*, *26*(6), 940–956. https://doi.org/10.1175/WAF-D-11-00002.1

Lombardo, K. A., & Colle, B. A. (2012). Ambient conditions associated with the maintenance and decay of quasi-linear convective systems crossing the northeastern U.S. coast. *Monthly Weather Review*, *140*(12), 3805–3819. https://doi.org/10.1175/MWR-D-12-00050.1

Lombardo, K. A., & Colle, B. A. (2013). Processes controlling the structure and longevity of two quasi-linear convective systems crossing the southern New England coast. *Monthly Weather Review*, *141*(11), 3710–3734. https://doi.org/10.1175/MWR-D-12-00336.1

Lombardo, K. A., & Kading, T. (2018). The behavior of squall lines in horizontally heterogeneous coastal environments. *Journal of the Atmospheric Sciences*, *75*(4), 1243–1269. https://doi.org/10.1175/JAS-D-17-0248.1

Lu, R., & Turco, R. P. (1994). Air pollutant transport in a coastal environment. Part I: Two-dimensional simulations of sea-breeze and mountain effects. *Journal of the Atmospheric Sciences*, *51*(15), 2285–2308. https://doi.org/10.1175/1520-0469(1994)051<2285:aptiac>2.0.co;2

Mahrer, Y., & Pielke, R. A. (1977). The effects of topography on sea and land breezes in a two-dimensional numerical model. *Monthly Weather Review*, *105*(9), 1151–1162. https://doi.org/10.1175/1520-0493(1977)105<1151:TEOTOS>2.0.CO;2

Mahrt, L. (1982). Momentum balance of gravity flows. *Journal of the Atmospheric Sciences*, *39*(12), 2701–2711. https://doi.org/10.1175/1520-0469(1982)039<2701:MBOGF>2.0.CO;2

Meng, Z., Yan, D., & Zhang, Y. (2013). General features of squall lines in East China. *Monthly Weather Review*, *141*(5), 1629–1647. https://doi.org/10.1175/MWR-D-12-00208.1

Morel, C., & Senesi, S. (2002). A climatology of mesoscale convective systems over Europe using satellite infrared imagery. II: Characteristics of European mesoscale convective systems. *Quarterly Journal of the Royal Meteorological Society*, *128*(584), 1973–1995. https://doi.org/10.1256/003590002320603494

Morrison, H., Milbrandt, J. A., Bryan, G. H., Ikeda, K., Tessendorf, S. A., & Thompson, G. (2015). Parameterization of cloud microphysics based on the prediction of bulk ice particle properties. Part II: Case study comparisons with observations and other schemes. *Journal of the Atmospheric Sciences*, *72*(1), 312–339. https://doi.org/10.1175/JAS-D-14-0066.1

Morrison, H., Thompson, G., & Tatarskii, V. (2009). Impact of cloud microphysics on the development of trailing stratiform precipitation in a simulated squall line: Comparison of one- and two-moment schemes. *Monthly Weather Review*, *137*(3), 991–1007. https://doi.org/10.1175/2008MWR2556.1

Olsson, L. E., Elliott, W. P., & Hsu, S.-I. (1973). Marine air penetration in Western Oregon: An observational study. *Monthly Weather Review*, *101*(4), 356–362. https://doi.org/10.1175/1520-0493(1973)101<0356:MAPIWO>2.3.CO;2

Parker, M. D., & Johnson, R. H. (2004). Simulated convective lines with leading precipitation. Part II: Evolution and maintenance. *Journal of the Atmospheric Sciences*, *61*(14), 1656–1673. https://doi.org/10.1175/1520-0469(2004)061<1656:SCLWLP>2.0.CO;2

Poulos, G. S., Bossert, J. E., McKee, T. B., & Pielke, R. A. (2000). The interaction of katabatic flow and mountain waves. Part I: Observations and idealized simulations. *Journal of the Atmospheric Sciences*, *57*(12), 1919–1936. https://doi.org/10.1175/1520-0469(2000)057<1919:TIOKFA>2.0.CO;2

Poulos, G. S., Bossert, J. E., McKee, T. B., & Pielke, R. A. (2007). The interaction of katabatic flow and mountain waves. Part II: Case study analysis and conceptual model. *Journal of the Atmospheric Sciences*, *64*(6), 1857–1879. https://doi.org/10.1175/JAS3926.1

Pucillo, A., Miglietta, M. M., Lombardo, K., & Manzato, A. (2019). *Application of a simple analytical model to severe winds produced by a bow echo like storm in northeast Italy* (pp. 1–18). Meteorological Applications. https://doi.org/10.1002/met.1868

Ralph, F. M., Venkateswaran, V., & Crochet, M. (1993). Observations of a mesoscale ducted gravity wave. *Journal of the Atmospheric Sciences*, *50*(19), 3277–3291. https://doi.org/10.1175/1520-0469(1993)050<3277:OOAMDG>2.0.CO;2

Ramis, C., & Romero, R. (1995). A first numerical simulation of the development and structure of the sea breeze on the Island of Mallorca. *Annales Geophysicae*, *13*(9), 981–994. https://doi.org/10.1007/s00585-995-0981-3

Román-Cascón, C., Yagüe, C., Viana, S., Sastre, M., Maqueda, G., Lothon, M., & Gómara, I. (2015). Near-monochromatic ducted gravity waves associated with a convective system close to the Pyrenees. *Quarterly Journal of the Royal Meteorological Society*, *141*(689), 1320–1332. https://doi.org/10.1002/qj.2441

Savijärvi, H., & Matthews, S. (2004). Flow over small heat islands: A numerical sensitivity study. *Journal of the Atmospheric Sciences*, *61*(7), 859–868. https://doi.org/10.1175/1520-0469(2004)061<0859:FOSHIA>2.0.CO;2

Wu, F., & Lombardo, K. (2021). Precipitation enhancement in squall lines moving over mountainous coastal regions. *Journal of the Atmospheric Sciences*, *78*(10), 3089–3113. https://doi.org/10.1175/JAS-D-20-0222.1

Yanai, M., Esbensen, S., & Chu, J.-H. (1973). Determination of bulk properties of tropical cloud clusters from large-scale heat and moisture budgets. *Journal of the Atmospheric Sciences*, *30*(4), 611–627. https://doi.org/10.1175/1520-0469(1973)030<0611:DOBPOT>2.0.CO;2